Available online at www.sciencedirect.com
SCIENCE DIRECT®
Journal of Solid State Chemistry 178 (2005) 882–891
JOURNAL OF SOLID STATE CHEMISTRY
www.elsevier.com/locate/jssc

Composition-induced structural phase transitions in the $(Ba_{1-x}La_x)_2In_2O_{5+x}$ $(0 \leqslant x \leqslant 0.6)$ system

C. Tenailleau[a,*], A. Pring[a], S.M. Moussa[a], Y. Liu[b], R.L. Withers[b], S. Tarantino[c], M. Zhang[c], M.A. Carpenter[c]

[a]*Department of Mineralogy, South Australian Museum, Earth Sciences Section, North Terrace, Adelaide, South Australia 5000, Australia*
[b]*Research School of Chemistry, Australian National University, Canberra, ACT 0200, Australia*
[c]*Department of Earth Sciences, University of Cambridge, Downing Street, Cambridge CB2 3EQ, UK*

Received 24 November 2004; received in revised form 5 January 2005; accepted 6 January 2005

Abstract

Composition-induced structural phase changes across the high temperature, fast oxide ion conducting $(Ba_{1-x}La_x)_2In_2O_{5+x}$, $0 \leqslant x \leqslant 0.6$, system have been carefully analysed using hard mode infrared (IR) powder absorption spectroscopy, X-ray powder diffraction and electron diffraction. An orthorhombic brownmillerite to three-dimensionally disordered cubic perovskite phase transition in this system is signalled by a drastic change in slope of both wavenumber and average line widths of IR spectra as a function of composition. Some evidence is found for the existence of an intermediate tetragonal phase (previously reported to exist from electron diffraction data) around $x \sim 0.2$. The new spectroscopic data have been used to compare microscopic and macroscopic strain parameters arising from variation in composition. The strain and spectroscopic data are consistent with first-order character for the tetragonal→orthorhombic transition, while the cubic→tetragonal transition could be continuous. Differences between the variation with composition of spectral parameters and of macroscopic strain parameters are consistent with a substantial order/disorder component for the transitions. There is also evidence for precursor effects within the cubic structure before symmetry is broken.

Keywords: IR powder absorption spectroscopy; Autocorrelation analysis; Perovskites; $(Ba_{1-x}La_x)_2In_2O_{5+x}$ solid solution; Phase transition; Electron diffraction; Strains

1. Introduction

Anion-deficient "defect fluorite" type materials, such as yttria-stabilized cubic zirconia, have long been the preferred materials of choice for use as high-temperature fast oxide ion conductors in a wide range of electrochemical devices such as oxygen sensors, solid oxide fuel cells and oxygen separation membranes. The ongoing need for new materials which exhibit comparable or, if possible, better fast oxide ion conductivity at even lower onset temperatures, however, has recently focussed attention on $A_2B_2O_5$ brownmillerite, and brownmillerite-related, phases (see, for instance, Refs. [1–14] and references contained therein).

The ideal brownmillerite structure type (*Ibm*2, $\mathbf{a}_o = \mathbf{a}_p - \mathbf{c}_p$, $\mathbf{b}_o = 4\mathbf{b}_p$, $\mathbf{c}_o = \mathbf{a}_p + \mathbf{c}_p$ in the setting most commonly used [3,5,7,9,14]; subscripts o for orthorhombic and p for parent perovskite here and in what follows) is an oxygen/vacancy ordered "defect perovskite" structure in which 1/6th of the oxygen ions of the ideal "defect perovskite" parent structure are replaced by an array of oxygen vacancies ordered into strings running along [101] directions in alternate (010) planes. This ordering scheme produces alternately octahedrally and tetrahedrally co-ordinated *B* (In) layers (cf. Fig. 1c with Fig. 1a). When heated to sufficiently high temperature, the oxygen vacancies (represented by the

*Corresponding author. Fax: 61 8 8207 7222.
E-mail address: christen@saugov.sa.gov.au (C. Tenailleau).

0022-4596/$ - see front matter © 2005 Elsevier Inc. All rights reserved.
doi:10.1016/j.jssc.2005.01.004

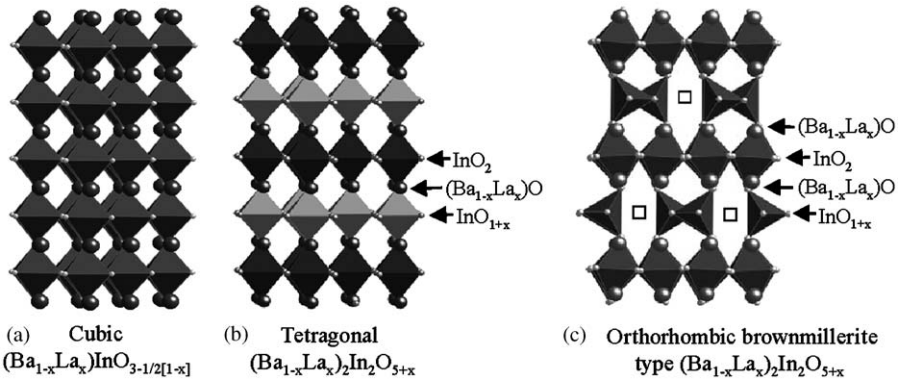

Fig. 1. Schematic diagrams of the (a) ideal cubic ($Pm\bar{3}m$) ABO_3 perovskite, (b) the proposed $1\times1\times2$ tetragonal ($P4/mmm$) "defect perovskite" superstructure phase and (c) orthorhombic ($Ibm2$) $A_2B_2O_5$ brownmillerite structure type, where $A=$ (Ba, La) and $B=$ In. BO_6 octahedra are in dark while the oxygen-deficient BO_4 and BO_{6-2y} polyhedra are in grey. The large grey balls and the open squares represent the A cations and oxygen vacancies, respectively.

open squares in Fig. 1c) become mobile, leading to high-temperature fast oxide ion conduction.

$Ba_2In_2O_5$, of orthorhombic *Ibm*2 (or *Icmm* [7]) brownmillerite structure type (see Fig. 1c) at room temperature, becomes a fast oxide ion conductor (with oxide ion conductivity comparable to that of the best-known "defect fluorite" oxide ion conductors, including yttria-stabilized zirconia [5]) above a well-defined first-order structural phase transition at ~925 °C apparent in calorimetry [2,12], ionic conductivity [1,4,5], NMR [2] and diffraction [2,3,7] data. ^{17}O NMR [2] and calorimetry [12] data show that this order/disorder phase transition involves the onset of oxide ion mobility, but only within the (two-dimensional) equatorial planes of the tetrahedral layers (see Fig. 1c). The high-temperature phase has a (intermediate) layered structure (see Fig. 1b), which has been reported as orthorhombic [2] but also as tetragonal [3]. The number of mobile oxide ions is then reported to increase continuously from ~925 to ~1075 °C. At ~1075 °C, all oxide ions are reported to become mobile, giving rise to a disordered cubic perovskite polymorph (see Fig. 1a) [2,3].

The desire to stabilize these high-temperature oxide ion conducting polymorph/s to room temperature has led to a variety of dopant schemes designed to lower, or even suppress altogether, the high-temperature phase transition/s (see, e.g., Refs. [5–11,13–15]). The focus of this paper is on a dopant scheme involving the replacement of Ba^{2+} ions with La^{3+} ions, leading to a coupled substitution of oxygen for vacancies and an overall stoichiometry $(Ba_{1-x}La_x)_2In_2O_{5+x}$ [8–11,14]. Uchimoto et al. [8,9] investigated the temperature-dependent ionic conductivity properties of this system. They reported the successful stabilization of the high-temperature cubic phase at room temperature for samples with $x\geqslant0.2$, as well as a continuously increasing oxide ion conductivity with increasing dopant level above $x=0.2$. Kakinuma et al. [10] confirmed the suppression of the ionic conductivity phase transition to room temperature for x somewhere between 0.1 and 0.2, and reported that the ionic conductivity for $x\geqslant0.4$ was higher than that of the best calcia- or yttria-stabilized zirconias [9].

With respect to crystal structure at room temperature in this system, Uchimoto et al. [8,9] reported a disordered $Pm\bar{3}m$, cubic "defect perovskite" structure for $x\geqslant0.2$ while Kakinuma et al. [10] reported orthorhombic symmetry for $0\leqslant x\leqslant0.3$, tetragonal symmetry for $0.3<x\leqslant0.5$ and cubic symmetry only for $0.5<x\leqslant0.6$. Mitome et al. [14] reported a multiply twinned, "…tetragonal brownmillerite structure…" for $x\geqslant0.1$ which only reverted to a cubic "defect perovskite" structure type in the vicinity of $x\sim0.5$. Finally, Liu et al. [11] reported a well-defined structural phase transition occurring somewhere between $x=0.1$ and 0.2 (correlating with the well-defined phase transition observed in the ionic conductivity versus x data [8–10]) from an orthorhombic brownmillerite structure type on the low x side to a multiply twinned, tetragonal (but very close to metrically cubic) $1\times1\times2$ perovskite-related superstructure phase on the high x side at 0.2. This tetragonal intermediate state was then reported to gradually transform to a disordered cubic phase for $x>0.2$.

The purpose of the present study was to investigate systematically the structural evolution of this $(Ba_{1-x}La_x)_2In_2O_{5+x}$, $0\leqslant x\leqslant0.6$, system as a function of x on a microscopic length scale using hard mode infrared (IR) powder absorption spectroscopy and, in particular, a recently developed autocorrelation analysis method [16]. The basic idea underlying the method is that any substitutions or disordering in a solid solution system will always cause local strains and structural relaxations that will be reflected in spectral line shifts and broadenings in IR spectra. It can be applied even to complex IR spectra containing broad peak overlapping,

as seen in many perovskite-related phases [17]. The method uses an autocorrelation function, defined as

$$\mathrm{Corr}(\alpha, w') = \int_{-\infty}^{+\infty} \alpha(\omega + \omega')\,\alpha(\omega)\,\mathrm{d}\omega, \quad (1)$$

where $\alpha(\omega)$ is the spectrum itself and $\alpha(\omega + \omega')$ is the same spectrum offset in frequency by ω', to extract and analyse spectral changes [16]. In theory, any peak position and/or width variation can be associated with individual lattice modes, polyhedral distortions and/or local heterogeneities in the structure. The spectroscopic data obtained can then be compared with, e.g., lattice parameter evolution as a function of composition and correlated to variations in macroscopic strains arising from composition-induced structural phase transitions.

2. Experimental

Specimens of $(Ba_{1-x}La_x)_2In_2O_{5+x}$, covering the composition range $0 \leqslant x \leqslant 0.6$, were carefully synthesized by conventional solid state methods. Stoichiometric proportions of the $BaCO_3$, La_2O_3 and In_2O_3 pre-dried raw materials were initially ground together in a mortar. The resultant mixtures were heat-treated at 1000 °C for 24 h, in order for decarbonation to take place. After further grinding, pellets were made and sintered for 48 h at either 1300 or 1400 °C (see Table 1), before quenching in cold water.

Table 1
Sample composition, sintering conditions and refined cell parameters from X-ray powder diffraction data of $(Ba_{1-x}La_x)_2In_2O_{5+x}$

x	Temperature (°C)	Symmetry	$\mathbf{a}_o$ (Å)	$\mathbf{b}_o$ (Å)	$\mathbf{c}_o$ (Å)
0	1250	*Icmm* (or *Icm*2)	6.100(1)	16.723(3)	5.961(1)
0.05	1300	*Icmm*	6.073(3)	16.703(7)	5.939(4)
0.10	1300	*Icmm*	6.055(2)	16.683(5)	5.949(3)
0.125	1300	*Icmm*	6.041(1)	16.676(3)	5.951(2)
0.15	1300	*Icmm*	6.029(2)	16.665(3)	5.947(2)
0.175	1300	*Icmm*	6.014(1)	16.689(3)	5.945(1)
0.20	1300	*P*4/*mmm*	4.1945(7)		8.389(8)
0.225	1300	*Pm*$\bar{3}$*m*	4.1801(8)		
0.25	1300	*Pm*$\bar{3}$*m*	4.1753(7)		
0.30	1300	*Pm*$\bar{3}$*m*	4.1680(5)		
0.40	1300	*Pm*$\bar{3}$*m*	4.1640(6)		
0.50	1300	*Pm*$\bar{3}$*m*	4.1586(5)		
0.60	1300	*Pm*$\bar{3}$*m*	4.1553(5)		
0.225	*1400*	*Pm*$\bar{3}$*m*	*4.1752(3)*		
0.25	*1400*	*Pm*$\bar{3}$*m*	*4.1738(8)*		
0.275	*1400*	*Pm*$\bar{3}$*m*	*4.1697(2)*		
0.30	*1400*	*Pm*$\bar{3}$*m*	*4.1629(3)*		
0.35	*1400*	*Pm*$\bar{3}$*m*	*4.1574(2)*		
0.40	*1400*	*Pm*$\bar{3}$*m*	*4.1531(6)*		
0.45	*1400*	*Pm*$\bar{3}$*m*	*4.1520(7)*		

The resultant products were investigated by X-ray powder diffraction using a Guinier–Hägg XRD camera with Cu$K\alpha$1 radiation. Silicon (NBS No.640) was added as an internal standard for accurate determination of the unit cell dimensions, which were refined using the "Unitcell" software package [18].

Electron diffraction experiments were carried out on finely ground materials dispersed onto holey carbon films using a Philips EM 430 instrument operating at 300 kV.

Twenty pellets for IR powder absorption spectroscopy were prepared, following a method developed previously [19] in order to obtain the best spectra for autocorrelation analysis. Initially, around 30 mg of each of the samples were ground separately for 15 min. After testing a number of potential sample grinding times and dilutions with CsI as a matrix, about 2 mg of the ground samples and ~300 mg of CsI (sample:matrix ratio of 1:150) were then mixed and pressed into pellets weighing ~300 mg. The mixtures were left for 7 min in a vacuum press before 13 mm diameter pellets were created under 10 tons of pressure.

A standard spectrum of pure CsI was obtained prior to measuring the primary IR spectra of CsI + sample. Data were collected (512 scans per spectrum) under vacuum at room temperature over two regions at an instrumental resolution of 2 cm^{-1} using a Bruker 113 V FT-IR spectrometer for the far-IR region (100–700 cm^{-1}) and a Bruker 66 V FT-IR spectrometer for the mid-IR region (400–2500 cm^{-1}).

3. Results and discussion

3.1. IR spectroscopy

The room-temperature IR powder absorption spectra of $(Ba_{1-x}La_x)_2In_2O_{5+x}$, $0 \leqslant x \leqslant 0.6$, in the mid- and far-IR regions are shown in Figs. 2 and 3, respectively. (The complementary data sets collected from the two spectrometers were treated separately for comparison purposes.) The three broad absorption bands visible at all compositions in the far-IR region (around 140, 320 and 590 cm^{-1}, respectively) are typical of a cubic perovskite structure type [20,21]. Following Ref. [20], the lowest frequency band (around 140 cm^{-1}) can be assigned to modes in which the Ba^{2+}/La^{3+} sub-lattice vibrates relative to the In^{3+} and O^{2-} ions, the mid-range band (around 320 cm^{-1}) to In–O bending modes and the highest frequency band (around 590 cm^{-1}) to In–O stretching modes. At low x, in the brownmillerite structure-type composition range, additional peaks (or "peak shoulders"), characteristic of lowered symmetry and additional IR-active modes, are apparent on each of these broad bands. The number of such modes progressively decreases as x, and the La content,

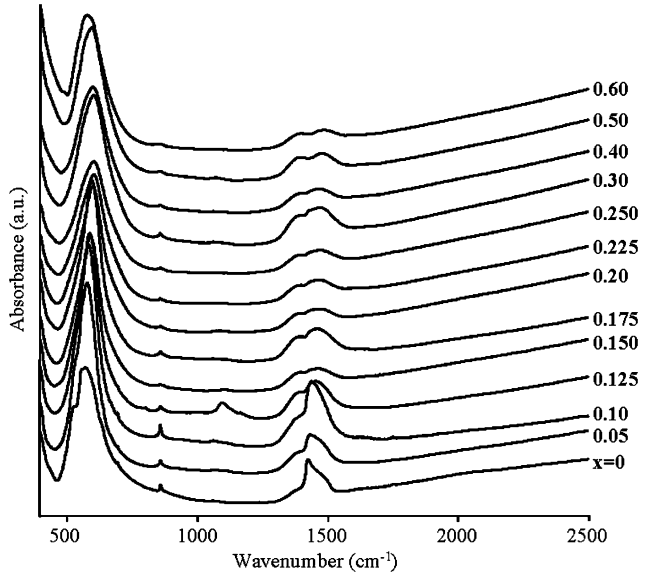

Fig. 2. IR powder absorption spectra at room temperature of $(Ba_{1-x}La_x)_2In_2O_{5+x}$, $0 \leqslant x \leqslant 0.6$ (mid-IR region).

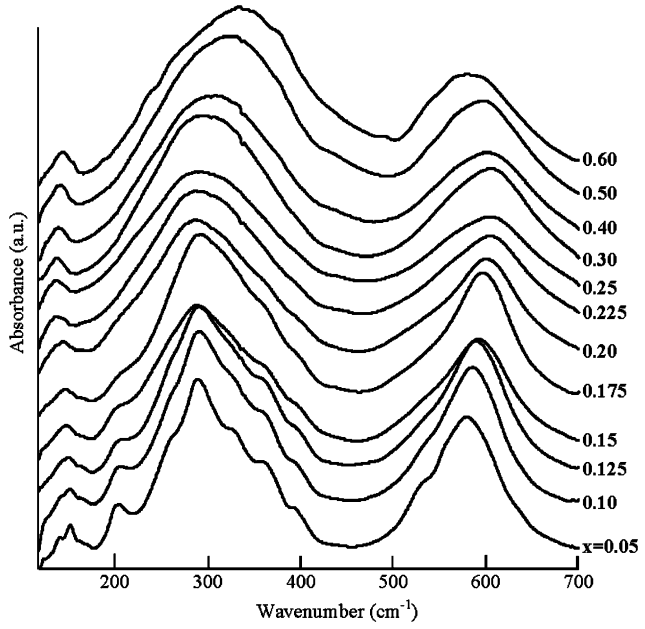

Fig. 3. IR powder absorption spectra at room temperature of $(Ba_{1-x}La_x)_2In_2O_{5+x}$, $0 \leqslant x \leqslant 0.6$ (far-IR region).

increases. They are no longer present for $x > 0.2$ where the symmetry has changed from orthorhombic to cubic (see Table 1). Note that the two additional lines (around 850 and 1450 cm^{-1}) observed at higher wavenumbers in the mid-IR region spectra (see Fig. 2) indicate the presence of a residual small amount of $BaCO_3$ presumably remaining in the samples after annealing [22].

Peak positions of the ~140 and ~600 cm^{-1} absorption bands, ω_{140} and ω_{600}, were obtained by calculating the first and second derivatives of the absorption signal using a computer routine and IGOR Pro software (Wavemetrics, Inc., Oregon, USA). The variations of ω_{600} with composition, x, are almost identical for spectra collected in the two different spectrometers (see Fig. 4a). The peak maximum is found to increase linearly with La content until $x \sim 0.225$, but then seems to stabilize just above this value before finally decreasing smoothly from $x = 0.3$ to 0.6. This change in the composition-dependent behaviour of the peak maximum correlates reasonably well with changes in the symmetry observed by XRD (cf. with Table 1). The wavenumber of the peak around 140 cm^{-1} decreases with increasing x until an abrupt change in behaviour occurs, again at around $x \sim 0.225$ (Fig. 4b). The variation of ω_{600} appears to be continuous through the whole composition range while ω_{140} possibly has a discontinuity between $x = 0.2$ and 0.225. The changes in wavenumber, $\delta\omega$, due to the structural changes associated with the cubic→orthorhombic symmetry are shown in Fig. 4c. For the calculation of $\delta\omega$, a linear extrapolation of data for the cubic phase was used.

In order to obtain more information about the influence of cation substitution on the structure of these materials, an effective line width Δ_{corr}, proportional to the average width of the peak(s) in the chosen segment of the primary spectrum, has been determined by autocorrelation analysis [16,17]. After subtracting a baseline for the spectral region analysed (keeping constant the number of points from one spectrum to another), a Gaussian curve, G, is used to fit to the central peak:

$$G = k_0 \exp\left[-((x - k_1)/k_2)^2\right], \quad (2)$$

where k_2 is proportional to the line width of the autocorrelation spectra. Δ_{corr} is then obtained by extrapolation of k_2 versus ω to the origin ($\omega' = 0$ in Eq. (1)). Fig. 5a shows the evolution of Δ_{corr} with La content calculated for the peak around 600 cm^{-1}, $\Delta_{corr600}$, from the mid-IR spectra and for the peak around 300 cm^{-1}, $\Delta_{corr300}$, from the far-IR spectra. Note that the autocorrelation method applied to the whole far-IR spectrum resulted in a pattern for Δ_{corr} with x which is identical to the pattern for $\Delta_{corr300}$. Note further that the scatter of Δ_{corr} data is significantly greater than the scatter for ω, implying that peak positions provide more tightly constrained measures of structural changes. Line widths can carry information about local structural heterogeneities as well as the behaviour of the average structure, however, and can yield additional insights into the mechanisms underlying solid solution formation [16,17,19]. The Δ_{corr} data produce well-defined linear trends for compositions at which $(Ba_{1-x}La_x)_2In_2O_{5+x}$ is cubic and then significant reductions in the range of the tetragonal/orthorhombic structures. The excess quantity, $\delta\Delta_{corr}$, defined in the same way as $\delta\omega$, shows the same pattern of variation with composition

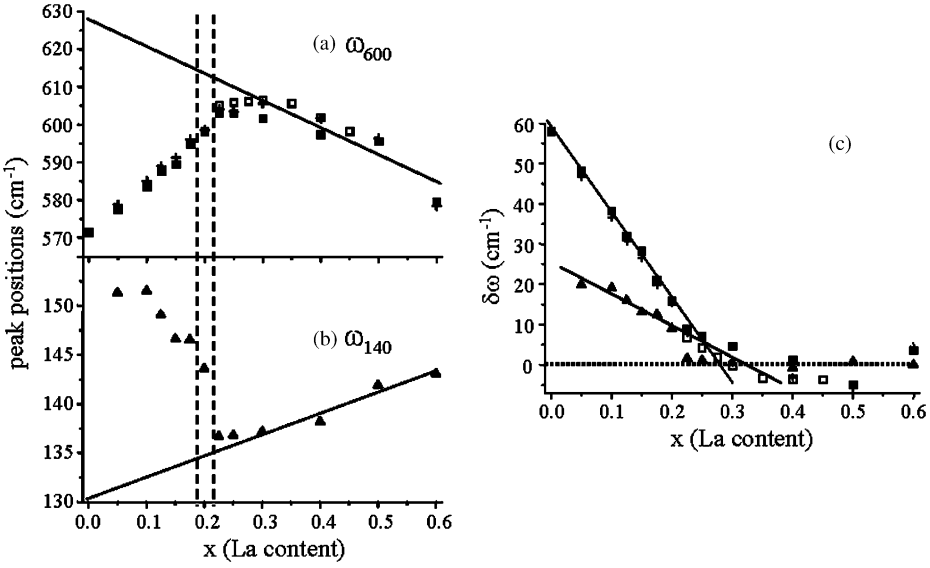

Fig. 4. Wavenumber of peaks around (a) 600 cm^{-1} from mid- (squares) and far- (crosses) IR regions and (b) 140 cm^{-1} (triangles) for $(Ba_{1-x}La_x)_2In_2O_{5+x}$ solid solutions as a function of composition. The empty squares correspond to the seven samples annealed for 2 days at 1400 °C. To clarify the figures and as the spectroscopic data obtained from the far-IR measurements for those seven samples are quasi-identical to the ones presented for the other samples of same composition, only the sample data determined from the mid-IR measurements (and for the peak positioned around 600 cm^{-1}) are presented in all figures for comparison. The full lines correspond to linear fits of values taken well in the cubic phase ($x \geqslant 0.3$). Vertical lines represent the approximate points of the transitions. (c) Magnitude of peak variations ($\delta\omega_{140}$ and $-\delta\omega_{600}$) against x, with symbols as in (a) and (b). The full lines correspond to linear fits of values from the orthorhombic phase ($x \leqslant 0.2$).

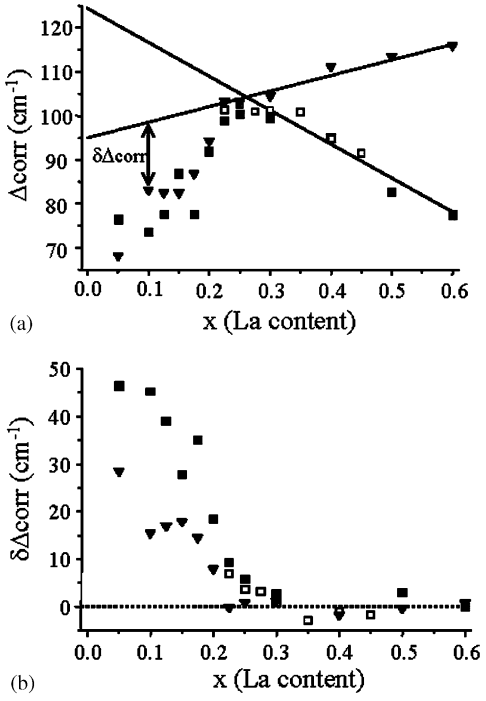

Fig. 5. (a) Variations of Δ_{corr} values calculated in the region around the peak at ~600 cm^{-1} (squares) and in the full far-IR measured area (down triangles). The open squares and straight lines are as defined for Fig. 3. (b) Excess line width parameter variations against x.

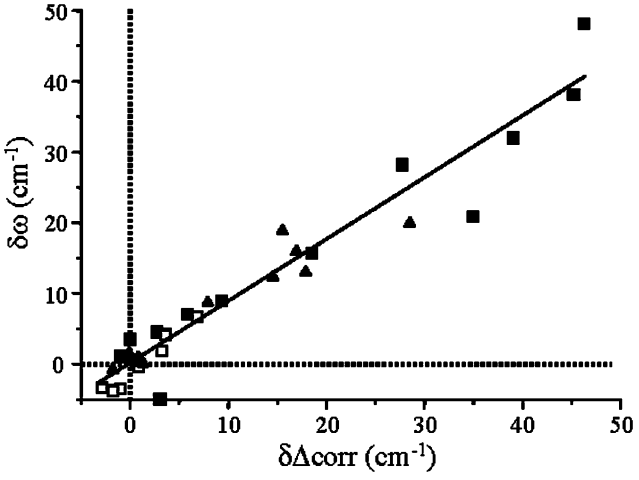

Fig. 6. Change in wavenumber for peaks around 600 and 140 cm^{-1} versus the excess line width parameters extracted from the mid- and far-IR region measurements. Symbols are as defined in Fig. 3.

(Fig. 5b) as seen in Fig. 4c. The two spectral parameters are linearly related, within experimental uncertainty (Fig. 6). In particular, the linear trends for the cubic structures imply that the disordered phase behaves as a more or less ideal solid solution (no excess properties), at least at the length scales sampled by IR spectroscopy. The excess properties, $\delta\omega$ and $\delta\Delta_{corr}$, of the hard modes are usually expected to scale with the square of the local order parameter, q, for a phase transition. All the data show a substantial break in slope at $x \sim 0.225$, but they do not define a linear trend which extrapolates to zero at this composition (as should be expected for a classical second-order transition).

3.2. Electron diffraction

Fig. 7 shows (a) [100] and (b) [001] zone axis electron diffraction patterns (EDPs) of the $x = 0.175$ sample ($\mathbf{a}_o = 6.014$, $\mathbf{b}_o = 16.689$, $\mathbf{c}_o = 5.945$ Å, see Table 1). These are typical of the $(Ba_{1-x}La_x)_2In_2O_{5+x}$, $0 \leqslant x \leqslant \sim 0.2$, brownmillerite-type solid solution field, and are consistent with either *Icmm* or *Icm*2 (*Ibm*2) symmetry ($F(hkl) = 0$ unless $(h + k + l)$ is even, due to the *I*-centered lattice; $F(0kl) = 0$ unless k and l are both even, due to the **c** glide). Evidence for average *Icmm* (rather than *Icm*2) symmetry can be found in the transverse polarized diffuse "streaking" (often a bit lumpy) running perpendicular to [001] along $\langle hk0 \rangle^*$ directions of reciprocal space (Figs. 8b, c and d). The transverse polarized nature of this diffuse streaking requires that atomic displacements (along **c**) must be responsible. Note that the diffuse streaking along $[\bar{1}10]^*$ apparent in the EDP which has a zone axis orientation close to $[1\bar{1}1]$ (Fig. 8b) vanishes when the zone axis orientation is exactly $[1\bar{1}1]$ (Fig. 8a).

Sheets of diffuse intensity perpendicular to **c** in reciprocal space (of which the observed $\langle hk0 \rangle^*$ diffuse streaking in Figs. 8b, c, and d constitute a part) imply the presence of real space columns of atoms along **c** whose displacements (primarily perpendicular to the diffuse streaking itself, i.e., along **c**) are correlated along **c** but with no correlation from column to column perpendicular to **c**. The most likely explanation of this structured diffuse scattering is displacive disorder within the one-dimensional corner-connected rows of InO_4 tetrahedra characteristic of the brownmillerite structure type (see Figs. 1 and 9). Consider, e.g., the disordered tetrahedral layers of $Ba_2In_2O_5$ when refined in *Icmm* [7] (see Fig. 9). Fig. 9 shows a single such disordered tetrahedral layer in projection along [010] in (a) and [001] in (b). The 50% occupied equatorial oxygen atom sites are those linked by the single-headed arrows in Fig. 9a. These sites are too close together to be simultaneously occupied either from one end of the arrow to the other or across the dashed line in Fig. 9a, i.e., within any one such [001] column, the equatorial oxygen atoms occupy either the positions at the beginning or at the end of the single-headed arrows in Fig. 9a. This gives rise to columns of corner-connected InO_4 tetrahedra running along the **c** direction in one or other of two possible orientations, one of which is outlined in black in Fig. 9a. It can be seen that these two different orientations could formally transform into one another via relatively simple, correlated translations of all the equatorial oxygen ions along **c** (the necessary shifts involved are represented by the single-headed arrows in Fig. 9a). In any one such column, one or other orientation is presumably occupied, with the other remaining unoccupied. If this happens in each column more or less independently of the neighbouring columns, it would give rise to transverse polarized sheets of diffuse intensity perpendicular to **c** just as is observed experimentally in the brownmillerite solid solution field (see Fig. 8).

The disappearance of $\langle hk0 \rangle^*$ diffuse streaking at exact zone axis orientations (cf. Fig. 8a with Fig. 8b) would also be explained by this displacively disordered proposal in that the 1d columns will necessarily superimpose on top of one another at such orientations. Any observed diffuse streaking will then reflect only the average displacements of the superposed 1d columns. These, however, could be expected to average to zero if there is no transverse correlation from one such column to the next. In a very real way, this proposed one-dimensional displacive disorder of the equatorial oxygen

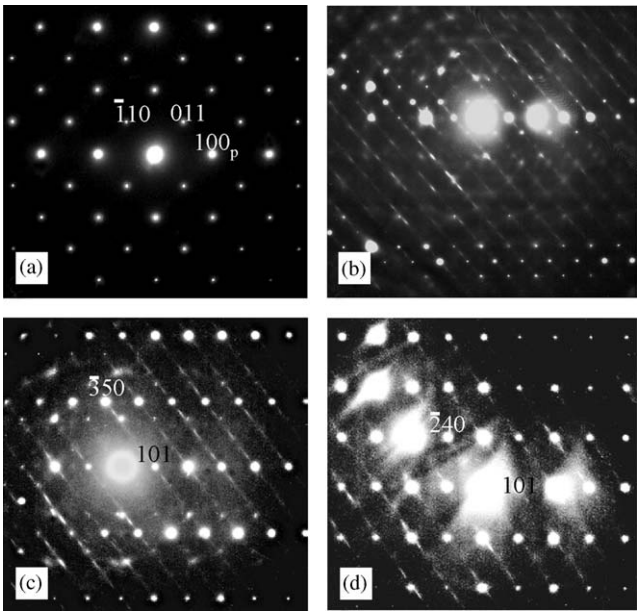

Fig. 8. (a) exact $[1\bar{1}1]$ and (b), (c) and (d) close to $[1\bar{1}1]$ zone axis EDPs of $(Ba_{1-x}La_x)_2In_2O_{5+x}$ with $x = 0.175$, showing transverse polarized diffuse streaking running perpendicular to [001] along $\langle hk0 \rangle^*$ directions of reciprocal space.

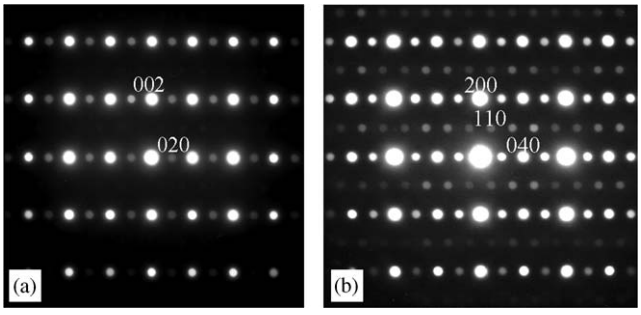

Fig. 7. (a) [100] and (b) [001] zone axis EDPs of $(Ba_{1-x}La_x)_2In_2O_{5+x}$ brownmillerite type, with $x = 0.175$, consistent with either *Icmm* or *Icm*2 (*Ibm*2) space groups.

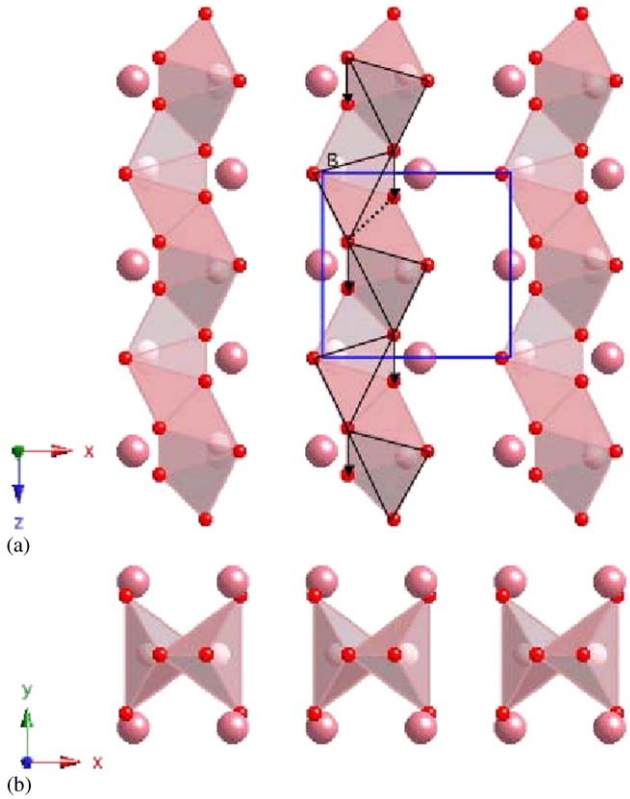

Fig. 9. Representation of the one-dimensional corner-connected rows of InO_4 tetrahedra characteristic of the brownmillerite structure type in projection along (a) [010] and (b) [001]. One of the two possible orientations for these corner-connected InO_4 tetrahedra is outlined in black. The large grey balls represent the A cations.

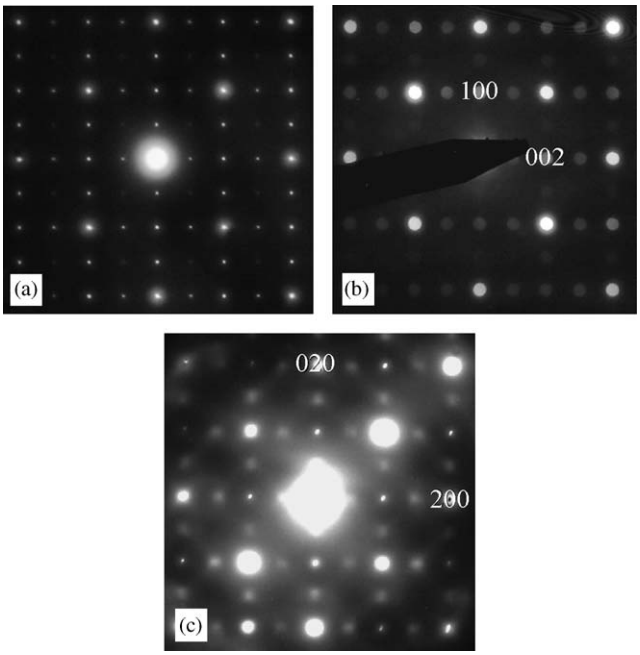

Fig. 10. (a) Typical $\langle 001 \rangle_p$-type selected area of EDP of the $x = 0.2$ sample along with (b) and (c) corresponding $\langle 001 \rangle_p$-type microdiffractions taken from a much smaller area showing the progressive disappearance of the $\mathbf{G} \pm \frac{1}{2}\langle 001 \rangle_p^*$ satellite reflections when x varies from $x = 0.2$ to 0.25.

ions of the tetrahedral layers can be thought of as the precursor to 1d liquid like behaviour along **c** of these oxygen ions.

The disappearance of the $\mathbf{G} \pm \frac{1}{4}\langle \bar{2}12 \rangle_p^*$ satellite reflections somewhere between $x = 0.175$ and 0.2 signals a well-defined brownmillerite to intermediate tetragonal ($\mathbf{a}_t = 4.1945(7)$, $\mathbf{c}_t = 8.389(8)$ Å), $P4/mmm$ phase transition (see Ref. [11]). This transition is clearly apparent in lattice parameter data (see Table 1) although only a few of the weak $\mathbf{G} \pm \frac{1}{2}\langle 001 \rangle_p^*$ superlattice reflections signalling the doubling of the $\mathbf{c}_p$ cell dimension are detectable in the XRD data. Note, however, that the subcell of the intermediate tetragonal phase remains very close to metrically cubic, leading to relatively fine scale twinning (cf. Figs. 10a and b) and making the subsequent intermediate tetragonal to disordered cubic transition rather difficult to detect from lattice parameter data alone. The $\mathbf{G} \pm \frac{1}{2}\langle 001 \rangle_p^*$ satellite reflections characteristic of the intermediate tetragonal phase are "sharp" at $x = 0.2$ (see Fig. 10a) but gradually become more diffuse on increasing x further until they transform into diffuse blobs around $x \sim 0.25$ (cf. Fig. 10a with Fig. 10c). This suggests that a tetragonal to cubic "transition" takes place somewhere between $x = 0.2$ and 0.25.

The cubic "defect perovskite" phase is characterized by a fascinating and highly structured diffuse intensity distribution (see, e.g., the (a) $[\bar{5}51]$ zone axis EDP of an $x = 0.5$ sample shown in Fig. 11a and the $\sim[\bar{1}20]$ zone axis EDP of an $x = 0.4$ specimen shown in Fig. 11b; see also Fig. 6 of Ref. [11]) suggesting the existence of strong local short-range ordering and associated structural relaxation. The detailed interpretation of such a complex diffuse intensity distribution, however, is well beyond the scope of the current contribution.

3.3. Group–subgroup and theoretical considerations

With the unit cell settings described below, $P4/mmm$ is a normal symmetry subgroup of $Pm\bar{3}m$ and $Icmm$ is a normal symmetry subgroup of $P4/mmm$. From the group theory tables of Stokes and Hatch [23], both the cubic → tetragonal and tetragonal → orthorhombic transitions are then permitted by symmetry to have second-order character. They are both also improper ferroelastic transitions. At high x the oxygen vacancy disordered, $Pm\bar{3}m$, $\mathbf{a} = \mathbf{a}_p$, $\mathbf{b} = \mathbf{b}_p$, $\mathbf{c} = \mathbf{c}_p$ cubic "defect perovskite" structure is stable (see Fig. 1a). On lowering of x to around $x \sim 0.225$, a $\mathbf{q} = \frac{1}{2}\mathbf{c}_p^*$ mode associated with oxygen vacancy localization into alternate equatorial (001) oxygen planes first condenses out (see Fig. 1b),

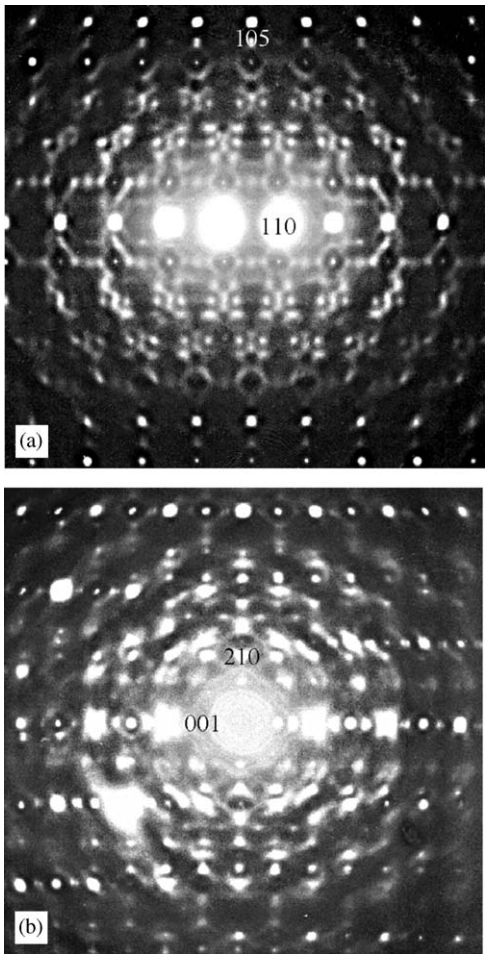

Fig. 11. (a) $[\bar{5}51]$ zone axis EDP of the $x = 0.5$ cubic sample and (b) $\sim[\bar{1}20]$ zone axis EDP of the $x = 0.4$ cubic specimen. Note the highly structured complex diffuse intensity distribution accompanying the strong Bragg reflections of the underlying "defect perovskite" cubic average structure.

giving rise to the tetragonal $P4/mmm$ ($\mathbf{a}_t = \mathbf{a}_p$, $\mathbf{b}_t = \mathbf{b}_p$, $\mathbf{c}_t = 2\mathbf{c}_p$) intermediate state. At even lower x's, a further frozen-in $\mathbf{q} = \frac{1}{2}[111]^*_t = \frac{1}{4}[221]^*_p$ mode condenses out. This is believed to be associated with further ordering of the oxygen vacancies into alternate fully occupied and partially occupied $[110]_p$ strings (see Fig. 1c). This yields the final resultant orthorhombic *Icmm* ($\mathbf{a}_o' = \mathbf{a}_t + \mathbf{b}_t = \mathbf{a}_p + \mathbf{b}_p$, $\mathbf{b}_o' = -\mathbf{a}_t + \mathbf{b}_t = -\mathbf{a}_p + \mathbf{b}_p$, $\mathbf{c}_o' = 2\mathbf{c}_t = 4\mathbf{c}_p$) brownmillerite-type structure. Note that while the *Icmm* space group symmetry in this setting is the same as that normally used, the two settings are quite distinct; the long axis is the **c** axis in this setting whereas the long axis is the **b** axis in the normally used setting. The transformation between the two is as follows: $\mathbf{a}_o' = \mathbf{a}_o$, $\mathbf{b}_o' = \mathbf{c}_o$ and $\mathbf{c}_o' = \mathbf{b}_o$. For the purposes of spontaneous strain calculations (see below), it is important to use the setting just described. Note that Table 1 lists $\mathbf{a}_o$, $\mathbf{b}_o$ and $\mathbf{c}_o$ in the case of the orthorhombic phase.

3.4. Lattice parameters and spontaneous strains

The refined cell parameters at room temperature for each composition, as determined by XRD, are given in Table 1. The values are in good agreement with data previously reported for *Icmm* (or *Icm*2), $P4/mmm$ and $Pm\bar{3}m$ space group symmetries for the orthorhombic, tetragonal and cubic phases, respectively [11].

In order to calculate the various components of the spontaneous-strain tensor describing the successive metric distortions of the cubic parent perovskite lattice, it is first necessary to define pseudo-cubic cell parameters $\mathbf{a} = \mathbf{a}_t$, $\mathbf{b} = \mathbf{a}_t$ and $\mathbf{c} = \mathbf{c}_t/2$ for the tetragonal phase and $\mathbf{a} = \mathbf{a}_o'/\sqrt{2} = \mathbf{a}_o/\sqrt{2}$, $\mathbf{b} = \mathbf{b}_o'/\sqrt{2} = \mathbf{c}_o/\sqrt{2}$ and $\mathbf{c} = \mathbf{c}_o'/4 = \mathbf{b}_o/4$ for the orthorhombic phase. Note that we have had to reset the usual setting of the orthorhombic brownmillerite phase in order to be compatible with the above group–subgroup relationships. These are shown plotted as a function of composition x in Fig. 12. A systematic volume contraction with increasing x is observed in both the orthorhombic brownmillerite and cubic "defect perovskite" solid solution fields, arising from the increasing proportion of the rather smaller La^{3+} ions relative to the larger Ba^{2+} ions in the average perovskite A sites.

From the general equations of Schlenker et al. [24], the trace components of the spontaneous-strain tensor are defined as

$$e_{11} = a/a_p - 1, \quad e_{22} = b/a_p - 1, \quad e_{33} = c/a_p - 1, \quad (3)$$

where the cubic reference a_p is given by a straight line fit to the data for $x > 0.25$ ($a_p = 4.176–0.03972x$). The degenerate symmetry-breaking strains related to orthorhombic and tetragonal distortions are given by

$$e_o = e_{11} - e_{22} \quad \text{and} \quad e_t = (2e_{33} - e_{11} - e_{22})/\sqrt{3}, \quad (4)$$

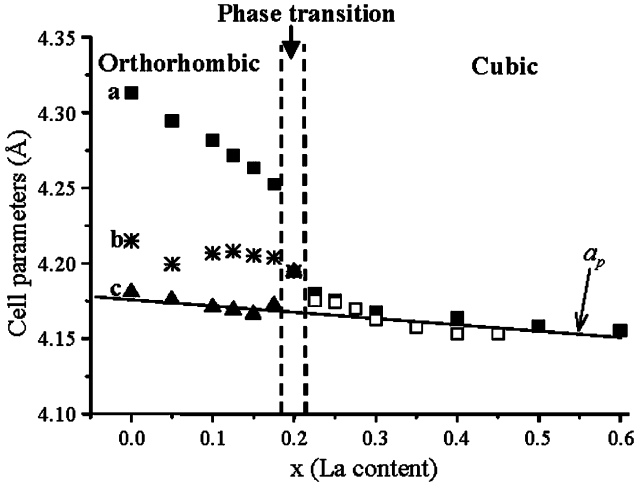

Fig. 12. Variations at room temperature in unit cell parameters of $(Ba_{1-x}La_x)_2In_2O_{5+x}$ with composition. Vertical lines represent the approximate points of the transitions. The full line corresponds to linear baseline used to determine a_p (determined for $x > 0.25$).

respectively, while the symmetry-adapted form of the non-symmetry-breaking strain is described by

$$e_a = e_{11} + e_{22} + e_{33}. \quad (5)$$

For an improper ferroelastic transition, both symmetry-breaking and non-symmetry-breaking strains are expected to scale with the square of the macroscopic order parameter, Q.

The experimentally observed strain behaviour of the $(Ba_{1-x}La_x)_2In_2O_{5+x}$ system (at room temperature) is shown in Fig. 13. The spontaneous strains accompanying the transformation from the orthorhombic brownmillerite to the cubic phase are remarkably large (around 2.5% for e_o, e_t and 4.5% for e_a (cf. Fig. 13a)) by comparison with previously studied perovskite-related phase transitions (see, e.g., Ref. [17]). There is a discontinuity in both e_o and e_t between $x = 0.175$ and 0.20 showing that the tetragonal→orthorhombic transition is first order in character. There is also some suggestion of a precursor volume strain in the cubic samples with composition close to the transition, though this interpretation is somewhat subjective in that it depends on the exact choice of baseline, a_p.

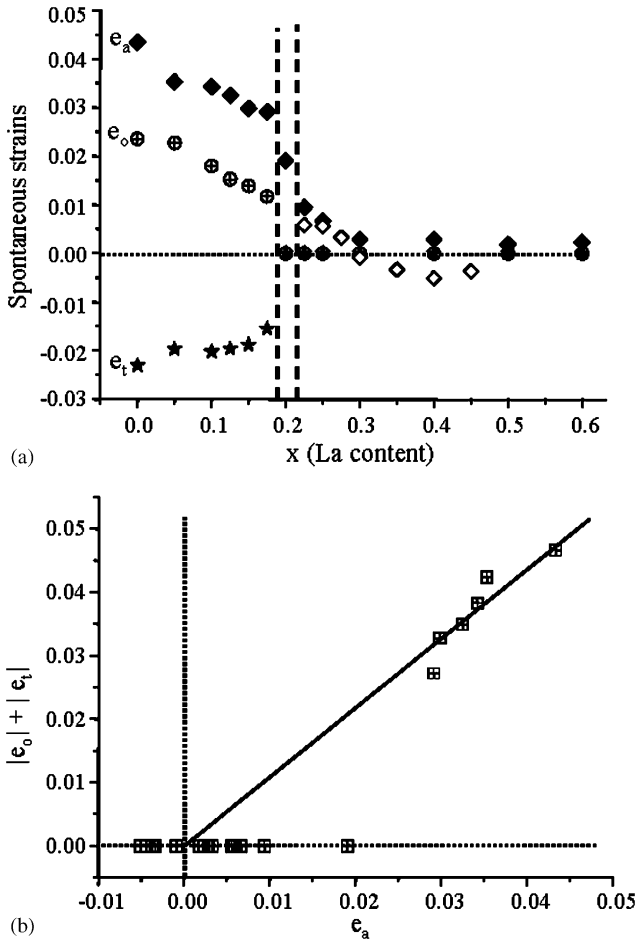

Fig. 13. Strain behaviour at room temperature of $(Ba_{1-x}La_x)_2In_2O_{5+x}$ solid solutions. (a) Variations of the orthorhombic, e_o (crossed circle), and tetragonal, e_t (star), shear strains and the volume strain, e_a (diamond (empty when one of the seven samples annealed for 2 days at 1400 °C)), with respect to a cubic structure, as a function of composition. Vertical lines represent the approximate points of transitions. (b) Variations of shear strains against volume strain. The straight line is a linear fit to the data, constrained to pass through the origin.

The cubic→tetragonal and tetragonal→orthorhombic transitions are associated with different special points in the Brillouin zone of the parent cubic structure, and the macroscopic strains are expected to couple with two separate order parameters, Q_t and Q_o, respectively. The magnitudes of e_o ($\propto Q_o^2$) and e_t ($\propto Q_t^2$) are approximately the same, however, implying that Q_o and Q_t vary in a strongly interdependent manner. The sum $|e_o| + |e_t|$ also varies linearly with e_a (Fig. 13b), consistent with $e_a = AQ_t^2 + BQ_o^2$, where A and B are coefficients representing combinations of strain/order parameter coupling coefficients and the elastic constants (of the reference cubic structure). The development of some volume strain ahead of the transition (Fig. 13a) would then imply that short-range order or dynamical effects relating to the orthorhombic structure occur even in the cubic or tetragonal phases. The diffuse intensity in diffraction patterns from the cubic phase (Fig. 11) is also indicative of some short-range order or dynamical effects away from the transition point.

Comparison of the spectroscopic data and spontaneous strains should provide some insights into the nature of the driving mechanisms at the different length scales sampled by each method. In the limit of a displacive mechanism, the local order parameter, q, at a phonon length scale will evolve in the same way as the macroscopic order parameter, Q. For the limiting case of an order/disorder transition, substantial short-range order may be achieved before the macroscopic symmetry is broken and q will evolve quite differently from Q. The tetragonal→orthorhombic transition is known to involve a marked increase in disorder accompanying an increase in oxygen ion mobility. It is not surprising, therefore, that the spectroscopic parameters, $\delta\omega$ and $\delta\Delta_{corr}$, show somewhat different variations with x than the strain parameters (compare Fig. 4c with Fig. 13a). In particular, changes in the spectral parameters are more or less continuous through both transitions, while the shear strains have marked discontinuities at the tetragonal→orthorhombic transition. The volume strain is more similar to the spectral parameters and both are presumably reflecting variations in local short-range order ahead of the transition as well as within the stability field of the orthorhombic structure.

4. Conclusion

Examination of the "defect perovskite" structure type of $(Ba_{1-x}La_x)_2In_2O_{5+x}$ by IR spectroscopy, strain

analysis and electron diffraction reveals details of the overall transformation behaviour driven by changes in composition. The $Pm\bar{3}m \rightarrow P4/mmm$ transition could be continuous but the $P4/mmm \rightarrow Icmm$ transition is first order in character. The spontaneous strains are large, particularly in the orthorhombic structure, indicating large structural relaxation associated with the transformation process. Differences between microscopic and macroscopic order parameter development are consistent with order/disorder mechanism while a possible precursor volume strain implies that significant local ordering effects occur in the stability field of the cubic structure.

Acknowledgments

The authors wish to thank the financial assistance of the Australian Research Council.

References

[1] J.B. Goodenough, J.E. Riuz-Diaz, Y.S. Zhen, Solid State Ionics 44 (1990) 21.
[2] S.B. Adler, J.A. Reimer, J. Baltisberger, U. Werner, J. Am. Chem. Soc. 116 (1994) 675.
[3] S.A. Speakman, J.W. Richardson, B.J. Mitchell, S.T. Misture, Solid State Ionics 149 (2002) 247.
[4] G.B. Zhang, D.M. Smyth, Solid State Ionics 82 (1995) 161.
[5] K.R. Kendall, C. Navas, J.K. Thomas, H.-C. zur Loye, Solid State Ionics 82 (1995) 215.
[6] K. Kakinuma, H. Yamamura, H. Haneda, T. Atake, Solid State Ionics 154–155 (2002) 571.
[7] P. Berastegui, S. Hull, F.J. Garcia-Garcia, S.-G. Eriksson, J. Solid State Chem. 164 (2002) 119.
[8] Y. Uchimoto, T. Yao, H. Takagi, T. Inagaki, H. Yoshida, Electrochemistry 68 (2000) 531.
[9] Y. Uchimoto, H. Takagi, T. Yao, N. Ozawa, T. Inagaki, H. Yoshida, J. Synchrotron. Radiat. 8 (2001) 857.
[10] K. Kakinuma, H. Yamamura, H. Haneda, T. Atake, Solid State Ionics 140 (2001) 301.
[11] Y. Liu, R.L. Withers, J.D. Fitz Gerald, J. Solid State Chem. 170 (2003) 247.
[12] T.R. Prasanna, A. Navrotsky, J. Mater. Res. 8 (1993) 1484.
[13] T. Yao, Y. Uchimoto, M. Kinuhata, T. Inagaki, H. Yoshida, Solid State Ionics 132 (2000) 189.
[14] M. Mitome, M. Okamoto, Y. Bando, H. Yamamura, J. Vac. Sci. Technol. B 19 (2001) 2284.
[15] H. Yamamura, Y. Yamada, T. Mori, T. Atake, Solid State Ionics 108 (1998) 377.
[16] E.K.H. Salje, M.A. Carpenter, T. Malcherek, T. Boffa Ballaran, Eur. J. Miner. 12 (2000) 503.
[17] H.-W. Meyer, M.A. Carpenter, A.I. Becerro, F. Seifert, Am. Miner. 87 (2002) 1291.
[18] B. Noläng, Inst. Materialkemi, Ångströmlaboratoriet, Box 538, S-751 21 Uppsala, Sweden.
[19] M. Zhang, B. Wruck, A. Graeme-Barber, E.K.H. Salje, M.A. Carpenter, Am. Miner. 81 (1996) 92.
[20] I. Nakagawa, A. Tsuchida, T. Shimanouchi, J. Chem. Phys. 47 (1967) 982.
[21] D.A. Crandles, T. Timusk, J.D. Garrett, J.E. Greedan, Phys. Rev. B 49 (1994) 4299.
[22] U. Rodehorst, M.A. Carpenter, S. Marion, C.M.B. Henderson, Min. Mag. 67 (2003) 989.
[23] H.T. Stokes, D.M. Hatch, Isotropy Subgroups of the 230 Crystallographic Space Groups, World Scientific, Singapore.
[24] J.L. Schlenker, G.V. Gibbs, M.B. Boisen Jr., Acta Crystallogr. A 34 (1978) 52.